The Journal of Chemical Physics

Experimental determination of the interaction potential between a helium atom and the interior surface of a C_{60} fullerene molecule

Cite as: J. Chem. Phys. **155**, 144302 (2021); https://doi.org/10.1063/5.0066817
Submitted: 12 August 2021 • Accepted: 17 September 2021 • Published Online: 11 October 2021

George Razvan Bacanu, Tanzeeha Jafari, Mohamed Aouane, et al.

The Journal of Chemical Physics ARTICLE scitation.org/journal/jcp

Experimental determination of the interaction potential between a helium atom and the interior surface of a C_{60} fullerene molecule

Cite as: J. Chem. Phys. 155, 144302 (2021); doi: 10.1063/5.0066817
Submitted: 12 August 2021 • Accepted: 17 September 2021 •
Published Online: 11 October 2021

George Razvan Bacanu,[1] Tanzeeha Jafari,[2] Mohamed Aouane,[3] Jyrki Rantaharju,[1] Mark Walkey,[1] Gabriela Hoffman,[1] Anna Shugai,[2] Urmas Nagel,[2] Monica Jiménez-Ruiz,[3] Anthony J. Horsewill,[4] Stéphane Rols,[3] Toomas Rõõm,[2] Richard J. Whitby,[1] and Malcolm H. Levitt[1,a)]

AFFILIATIONS

[1] School of Chemistry, University of Southampton, Southampton SO17 1BJ, United Kingdom
[2] National Institute of Chemical Physics and Biophysics, Tallinn 12618, Estonia
[3] Institut Laue-Langevin, BP 156, 38042 Grenoble, France
[4] School of Physics and Astronomy, University of Nottingham, Nottingham NG7 2RD, United Kingdom

[a)] **Author to whom correspondence should be addressed:** mhl@soton.ac.uk

ABSTRACT

The interactions between atoms and molecules may be described by a potential energy function of the nuclear coordinates. Nonbonded interactions between neutral atoms or molecules are dominated by repulsive forces at a short range and attractive dispersion forces at a medium range. Experimental data on the detailed interaction potentials for nonbonded interatomic and intermolecular forces are scarce. Here, we use terahertz spectroscopy and inelastic neutron scattering to determine the potential energy function for the nonbonded interaction between single He atoms and encapsulating C_{60} fullerene cages in the helium endofullerenes ^{3}He@C_{60} and ^{4}He@C_{60}, synthesized by molecular surgery techniques. The experimentally derived potential is compared to estimates from quantum chemistry calculations and from sums of empirical two-body potentials.

I. INTRODUCTION

Nonbonded intermolecular interactions determine the structure and properties of most forms of matter. The *potential energy function* specifies the dependence of the potential energy on the nuclear coordinates of the interacting moieties within the Born–Oppenheimer approximation.[1] The estimation of potential functions for nonbonded interactions remains an active research area of computational chemistry.[2–4] *Ab initio* methods are capable of high accuracy but are usually too computationally expensive to be applied to anything but very small molecular systems. Computational techniques with good scaling properties, such as density functional theory (DFT), are generally imprecise for nonbonded interactions, unless customized adjustments are made.[3–5] The accuracy of quantum chemistry algorithms is often assessed by seeking convergence with respect to the calculation level or number of basis functions.[2]

Advances in all fields of science require comparison with experiment. Unfortunately, detailed experimental data on intermolecular potential energy surfaces are scarce. Some information may be gained by comparing crystal structures and energetics with those derived from model potentials.[6] The equilibrium structures, dissociation energies, and vibrational frequencies of intermolecular complexes and clusters may be studied in the gas phase and molecular beams.[7–12] However, these measurements encounter difficulties with control of the local sample temperature and only provide information on potential minima and their local properties close to potential minima (unless tunneling splittings are resolved). Atomic beam diffraction may also provide information.[13–15]

An ideal set of systems for the study of intermolecular interactions is provided by atomic and molecular endofullerenes, in which single atoms or small molecules are encapsulated in closed carbon cages.[16–19] A range of small-molecule endofullerenes is available in macroscopic quantities through the multistep synthetic route

known as "molecular surgery,"[20] including $H_2@C_{60}$,[18] $H_2@C_{70}$,[21] $H_2O@C_{60}$,[19] $HF@C_{60}$,[22] $CH_4@C_{60}$,[23] and their isotopologues. Endofullerenes containing noble gas atoms and containing two encapsulated species may also be produced.[21,24–30] Endofullerenes are chemically very stable, may be prepared in a pure and homogeneous solid form, and may be studied at almost any desired temperature.

At low temperatures, the translational modes (and for non-monatomic species, the internal degrees of freedom) of the endohedral species are quantized. The quantum levels may be probed by a wide range of spectroscopic techniques,[31] including infrared spectroscopy,[22,32–36] pulsed terahertz spectroscopy,[37] nuclear magnetic resonance (NMR),[22,29,34,38–40] and inelastic neutron scattering.[22,34,41,42] When performed at cryogenic temperatures, these techniques reveal a rich energy level structure for the quantized modes of the encapsulated systems.[22,32,34,41,43] The quantum structure has been studied in detail using models of the confining potential, sometimes combined with cage-induced modifications of the rotational and vibrational characteristics of the guest molecule.[32,33,35,36,43–56]

There are two main ways to describe the interaction potential between the encapsulated species and the cage. One approach describes the interaction potential as a sum over many two-body Lennard-Jones (LJ) functions involving each endohedral atom and all 60 carbon atoms of the cage,[44–46,49,50,52,53,55,56] sometimes introducing "additional sites" on the endohedral species as well.[46,52,53] One disadvantage of this approach is that the summed potential has an undesirable dependence on the precise radius of the encapsulating fullerene cage. An alternative approach, which we call "model-free," describes the interaction potential as a sum of orthogonal spatial functions.[32,33,35,36,43,47,48] The latter approach makes no assumptions about the cage geometry and is better suited for a comparison with computational chemistry methods.

In this report, we "go back to basics" by studying the simplest atomic endofullerene, $He@C_{60}$, consisting of C_{60} fullerene cages, each encapsulating a single helium atom [Fig. 1(a)]. Terahertz and neutron scattering data are acquired and fitted by a simple quantum mechanical model consisting of a particle confined by a three-dimensional potential well. This allows us to define a "model-free" atom-fullerene potential with no assumptions about whether it may be expressed as the sum of many two-body interactions.

Although $He@C_{60}$ was first made in trace amounts by gas phase methods,[16,17,57] molecular surgery techniques now provide both isotopologues $^3He@C_{60}$ and $^4He@C_{60}$ in high purity and macroscopic quantities.[25,30] These synthetic advances have made it feasible to perform terahertz spectroscopy and inelastic neutron scattering experiments on solid polycrystalline samples of $He@C_{60}$ at low temperatures with a good signal-to-noise ratio.

At first sight, $He@C_{60}$ is an unpromising object of study by both terahertz spectroscopy and neutron scattering. Since He atoms are neutral, their translational motion is not expected to interact with electromagnetic radiation. Furthermore, both ^3He and ^4He isotopes have small neutron scattering cross sections, and ^3He is a strong neutron absorber. Fortunately, although these concerns are valid, they are not fatal. An off-center He atom acquires a small induced electric dipole through its interactions with the encapsulating C_{60} cage, as is known for $H_2@C_{60}$.[32] The induced dipole is approximately linearly dependent on the displacement from the cage center, allowing the He atom to interact weakly with THz irradiation. The feeble neutron scattering of both He isotopes may be compensated by a sufficiently large sample quantity.

We compare the experimentally determined potential to estimates from empirical two-body interaction potentials and from quantum chemistry calculations. Empirical two-body potentials give widely divergent results, even when those potentials are based on experimental helium–graphite scattering data. Møller–Plesset perturbation (MP2) theory techniques and density functional theory (DFT) methods, which explicitly include, or are empirically corrected to account for, dispersive interactions, are shown to provide good estimates for the interaction potential.

II. MATERIALS AND METHODS

A. Sample preparation

$^3He@C_{60}$ and $^4He@C_{60}$ were synthesized using a solid-state process for the critical step, as described in Ref. 30. The initial filling factors were 30%–50%. The samples were further purified by recirculating high-performance liquid chromatography (HPLC) on Cosmosil Buckyprep columns to remove trace impurities of $H_2O@C_{60}$. Without this precaution, strong neutron scattering by the hydrogen nuclei interferes strongly with the INS measurements. For THz spectroscopy, samples of high filling factor were required to get sufficient signal and were prepared by further recirculating HPLC. All samples were sublimed under vacuum before spectroscopic measurements.

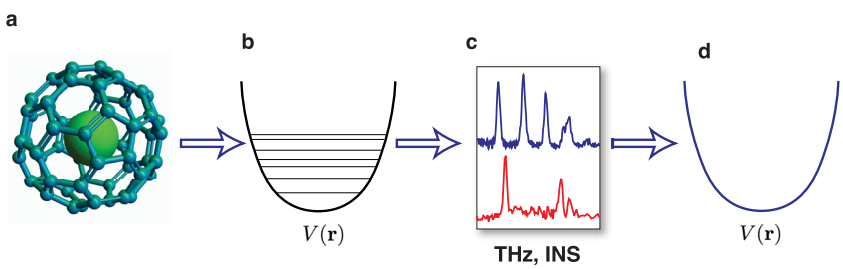

FIG. 1. (a) A C_{60} cage encapsulates a single noble gas atom. (b) The confinement potential of the encapsulated atom is described by the function $V(\mathbf{r})$. The quantum energy levels and wavefunctions of the encapsulated atom depend on $V(\mathbf{r})$. (c) Transitions between the energy levels are detected in the bulk solid state at low temperatures by terahertz spectroscopy and inelastic neutron scattering. (d) Analysis of the spectroscopic and neutron scattering data allows determination of the potential energy function, which may be compared with computational chemistry estimates.

B. Terahertz spectroscopy

THz absorption spectra were measured with an interferometer using a mercury arc light source and a 4 K bolometer as an intensity detector. The typical instrumental resolution was 0.3 cm^{-1}, which is below the width of the measured THz absorption lines. The $^4He@C_{60}$ sample had a filling factor of f = 88.2% ±0.5%, while the $^3He@C_{60}$ had a filling factor of f = 97.2% ±0.5%, as determined by ^{13}C NMR. The sample pellets were pressed from fine powders of solid $He@C_{60}$. The temperature dependence of the absorption spectra was measured by using a variable–temperature optical cryostat. More information is in the supplementary material.

C. Inelastic neutron scattering

INS experiments were conducted using the IN1-Lagrange spectrometer at the Institut Laue-Langevin (ILL) in Grenoble. Incident neutrons are provided by the "hot source" moderator of the reactor, resulting in a high flux neutron beam. A choice of three different single crystal monochromators, namely, Si(111), Si(311), and Cu(220), are used to define the incident energy of the monochromatic neutron beam arriving at the sample using Bragg reflection. The neutrons scattered by the interaction with the sample enter a secondary spectrometer comprising a large area array of pyrolytic graphite analyzer crystals. The focusing geometry of the secondary spectrometer ensures that only neutrons with a fixed kinetic energy of 4.5 meV are detected by the ^3He detector. INS spectra were recorded in the energy transfer range of [5, 200] meV for the $^3He@C_{60}$ sample, while it was reduced to [5, 60] meV for $^4He@C_{60}$ as the time allowed for performing the latter experiment was reduced.

The powdered samples with respective masses of 1067 mg for $^3He@C_{60}$ (f = 45%) and 294 mg for $^4He@C_{60}$ (f = 40%) were loaded inside an Al foil and further inserted inside a cylindrical annulus before they were mounted at the tip of an orange cryostat and placed inside the IN1 spectrometer beam. The sample temperature was kept around 2.7 K. In order to subtract background and scattering from Al and from the C_{60} cage, a blank mass matching sample of C_{60} was measured using the same setup and an empty cell was also measured. In order to account for the strong absorption of $^3He@C_{60}$, a Cd sample was also measured, enabling one to correct from the incident energy dependent absorption of the sample. The neutron counts in Fig. 3 were normalized to the incident neutron flux.

III. EXPERIMENTAL RESULTS

A. Terahertz spectroscopy

Terahertz absorption spectra for $^3He@C_{60}$ and $^4He@C_{60}$ at two different temperatures are shown in Fig. 2. For both isotopologues, the high-temperature spectrum displays a comb of several clearly resolved THz peaks, with the ^3He peaks having higher frequencies than those of ^4He. As discussed below, the combs of THz peaks indicate that the potential energy function $V(r)$ for the encapsulated He does not have a purely quadratic dependence on the displacement r of the He atom from the cage center. This indicates that the He dynamics is not well-described as a harmonic three-dimensional oscillator.

The 5 K spectra in Fig. 2 display a single peak with a partially resolved fine structure for both $^3He@C_{60}$ and $^4He@C_{60}$. These fundamental peaks correspond to transitions from the quantum ground

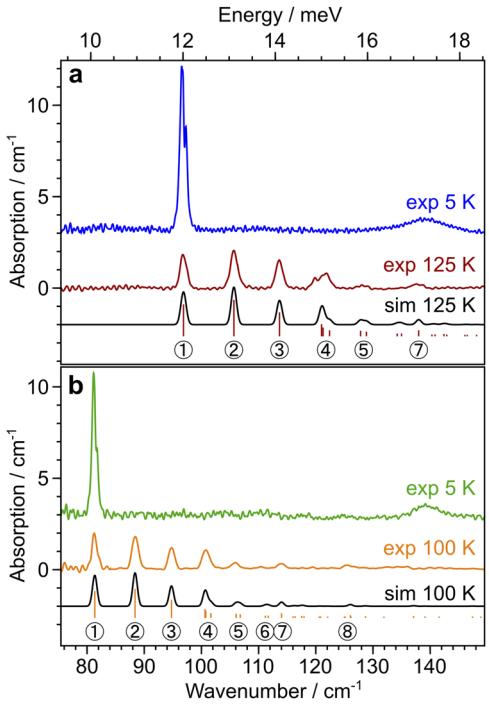

FIG. 2. THz spectroscopy of He endofullerenes. (a) THz absorption spectra of $^3He@C_{60}$ at temperatures of 5 K (blue) and 125 K (red). (b) THz absorption spectra of $^4He@C_{60}$ at temperatures of 5 K (green) and 100 K (orange). In both cases, the short vertical bars indicate the predicted positions of the terahertz absorption peaks for the radial potential energy function specified in Table I, and their height is proportional to the absorption area. In both cases, the black curve is the sum of Gaussian peaks with the position and area defined by the vertical bars. The THz peaks are numbered according to the transition assignments in Fig. 4(b).

states of He in the two isotopologues. The fine structure requires further investigation but may be associated with a small perturbation of the confining potential by the merohedral disorder in the crystal lattice, meaning the inhomogeneous orientations of neighboring C_{60} cages with respect to each other. Similar effects have been identified for $H_2@C_{60}$.[42]

B. Inelastic neutron scattering

Inelastic neutron scattering spectra for $^3He@C_{60}$ and $^4He@C_{60}$ are shown in Fig. 3. The figure shows the difference between the INS of the He endofullerenes and that of the pure C_{60}. The INS spectra before subtraction are shown in the supplementary material. Since C_{60} has no vibrational modes below ~ 250 cm^{-1}, and the low-energy phonon spectrum cancels precisely for the empty and filled fullerenes, the peaks below this energy threshold are clearly attributable to the quantized modes of the confined He atoms. As in the case of THz spectroscopy, the ^3He INS peaks are at higher energies than for ^4He.

The strong features above ~ 250 cm^{-1} are attributed to the known vibrational modes of C_{60} molecules.[58] Raman studies have shown that the radial vibrational modes of the C_{60} cages are slightly blue-shifted by the presence of an endohedral noble gas atom.[59]

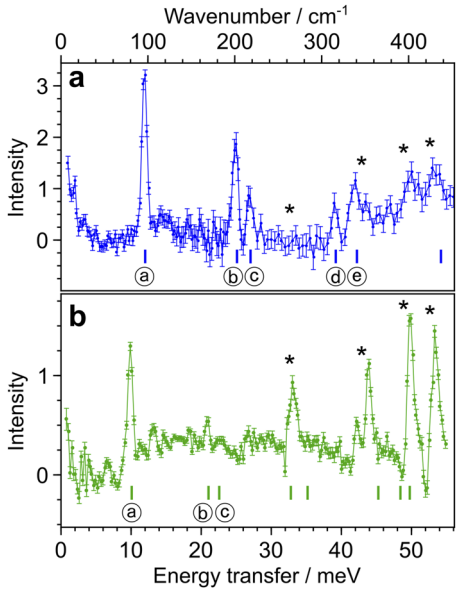

FIG. 3. Inelastic neutron scattering of He endofullerenes. (a) Inelastic neutron scattering spectra of ^{3}He@C_{60} at a temperature of 2.7 K (blue). (b) Inelastic neutron scattering spectra of ^{4}He@C_{60} at a temperature of 2.7 K (green). In both cases, a weighted difference between the scattering of He@C_{60} and pure C_{60} is shown, with the weighting factors adjusted for best subtraction of the C_{60} background. The short vertical bars indicate the predicted positions of the INS peaks for the quantized He motion under the radial potential energy function specified in Table I. The INS peaks are labeled according to the transition assignments in Fig. 4(b). The peaks above ~ 250 cm^{-1} and marked by asterisks are due to scattering from the C_{60} cages, whose modes are slightly modified in frequency by the presence of endohedral He.

These shifts lead to imperfect cancellation in the INS difference spectra, causing the dispersion-like features shown in Fig. 3, which are marked by asterisks. These subtraction artifacts are much stronger for ^{4}He than for ^{3}He for two reasons: (i) the C_{60} vibrational modes are slightly more shifted for ^{4}He than for ^{3}He due to its larger mass and (ii) ^{4}He has a much lower scattering cross section than ^{3}He. The poor signal-to-noise ratio for ^{4}He causes some of the expected peaks to be barely visible, an example being the peak marked "c" in Fig. 3(b).

IV. ANALYSIS

A. Energy levels and transitions

The Schrödinger equation for the confined atom (within the Born–Oppenheimer approximation) is given by

$$\hat{H}(\mathbf{r})\psi_{\mathbf{q}}(\mathbf{r}) = E_{\mathbf{q}}\psi_{\mathbf{q}}(\mathbf{r}), \tag{1}$$

where $\mathbf{q}$ describes a set of quantum numbers, $\mathbf{q} = \{q_1, q_2, \ldots\}$, and $E_{\mathbf{q}}$ is the energy of the stationary quantum state. The Hamiltonian operator $\hat{H}$ is given by

$$\hat{H}(\mathbf{r}) = -\frac{\hat{p}^2}{2M} + V(\mathbf{r}), \tag{2}$$

where $\hat{p}$ is the momentum operator and M is the atomic mass. In general, the energy levels $E_{\mathbf{q}}$ and stationary state wavefunctions $\psi_{\mathbf{q}}$ depend strongly on the potential energy function $V(\mathbf{r})$, where $\mathbf{r}$ represents the nuclear coordinates of the encapsulated atom [Fig. 1(b)].

Equations (1) and (2) assume that the cage coordinates are fixed and neglect environmental effects from beyond the cage—although the treatment may readily be extended to include the electrostatic influence of the lattice environment, as has been carried out for studies of H_2O@C_{60}.[36,51,55,56]

The potential energy of the He atom inside the cage may be described by a potential function $V(r, \theta, \phi)$, where r is the displacement of the He nucleus from the cage center and (θ, ϕ) are the polar angles. The C_{60} cage has icosahedral symmetry but may be treated as spherical to a good approximation at low excitation energies of the endohedral atom. The angular dependence may be dropped by assuming approximate spherical symmetry, $V(r, \theta, \phi) \simeq V(r)$. We assume a radial potential energy function of the form $V(r) = V_2 r^2 + V_4 r^4 + V_6 r^6$, where $\{V_2, V_4, V_6\}$ are the polynomial coefficients.

The energy eigenvalues and eigenstates are given by $E_{n\ell m}$ and $\psi_{n\ell m}(r, \theta, \phi)$, respectively. The principal quantum number n takes values $n \in \{0, 1, \ldots\}$ with the angular momentum quantum number ℓ given by $\ell \in \{0, 2, \ldots, n\}$ (for even n) and $\ell \in \{1, 3, \ldots, n\}$ (for odd n).[60] The azimuthal quantum number takes values $m \in \{-\ell, -\ell + 1, \ldots, +\ell\}$. For spherical symmetry, the energies are independent of m, so the energy level $E_{n\ell}$ is $(2\ell + 1)$-fold degenerate. The icosahedral cage symmetry introduces perturbation terms of spherical rank 6 and higher and only breaks the degeneracies of spherical states with large angular momentum quantum numbers. Within the spherical approximation, the stationary quantum states $\psi_{n\ell m}(r, \theta, \phi)$ are given by products of radial functions $R_{n\ell}(r)$ and spherical harmonics $Y_{\ell m}(\theta, \phi)$, just as for the electronic orbitals of a hydrogen atom.[60]

The eigenvalues and eigenstates depend on the potential coefficients $\{V_2, V_4, V_6\}$ and the mass of the He atom. The electric-dipole-allowed transitions, which are observed in THz spectroscopy and described by the induced dipole moment coefficient A_1, have the selection rule $\Delta\ell = \pm 1$; see the supplementary material. There are no relevant selection rules for the neutron scattering peaks.

B. Fitting of the potential

We treat the V_4 and V_6 terms as perturbations of the quadratic V_2 term, which corresponds to an isotropic three-dimensional harmonic oscillator. The solutions of the Schrödinger equation for the isotropic 3D harmonic oscillator are well-known[60,61] and are given by

$$|n\ell m\rangle(r, \theta, \phi) = R_{n\ell}(r) Y_{\ell m}(\theta, \phi), \tag{3}$$

where the principal quantum number is given by $n \in \{0, 1, 2, \ldots\}$ and the angular momentum quantum number ℓ takes values $\{0, 2, \ldots, n\}$ for even n and $\{1, 3, \ldots, n\}$ for odd n. The radial wavefunctions $R_{n\ell}(r)$ are proportional to generalized Laguerre polynomials,[62,63] while the angular parts $Y_{\ell m}$ are spherical harmonics. The energy eigenvalues are given by

$$E_{n\ell m} = \hbar\omega_0\left(n + \frac{3}{2}\right) \tag{4}$$

TABLE I. Best-fit polynomial coefficients and confidence limits for the radial potential function $V(r) = V_2 r^2 + V_4 r^4 + V_6 r^6$ and induced dipole function $d_{1q} = \sqrt{4\pi/3}\, A_1\, r\, Y_{1q}(\theta, \phi)$ experienced by the confined He isotopes; see the supplementary material.

Parameter	^{3}He	^{4}He
V_2 (meV pm^{-2})	$(2.58 \pm 0.06) \times 10^{-3}$	$(2.50 \pm 0.05) \times 10^{-3}$
V_4 (meV pm^{-4})	$(3.37 \pm 0.15) \times 10^{-7}$	$(3.61 \pm 0.11) \times 10^{-7}$
V_6 (meV pm^{-6})	$(2.79 \pm 0.12) \times 10^{-11}$	$(2.63 \pm 0.09) \times 10^{-11}$
A_1 (D pm^{-1})	$(4.38 \pm 0.09) \times 10^{-4}$	$(4.58 \pm 0.06) \times 10^{-4}$

with the fundamental vibrational frequency $\omega_0 = (2V_2/\mu)^{1/2}$, where μ is the reduced mass (assumed here to be equal to the mass of the ^{3}He or ^{4}He atoms, since each C_{60} molecule is more than two orders of magnitude more massive than the encapsulated atom and is also coupled to the lattice).

The Schrödinger equation was solved approximately for finite V_4 and V_6 by numerically diagonalizing a matrix with elements given by $\langle n\ell m|V_4 r^4 + V_6 r^6|n'\ell' m'\rangle$. Since the assumed Hamiltonian retains isotropic symmetry, all matrix elements are independent of the quantum number m and vanish for $\ell \neq \ell'$ and $m \neq m'$. In practice, the matrix was bounded by the quantum numbers $n \leq 18$ after checking for convergence. The THz peak intensities and peak positions were fitted, as described in the supplementary material, allowing numerical estimation of the potential parameters V_2 (or ω_0), V_4, and V_6 and the induced dipole moment amplitude A_1. The derived eigenvalues were used to estimate the INS peak positions.

The fitting of the potential was performed independently for the two He isotopes. The best-fit solutions for the potential coefficients and their confidence limits are given in Table I.

Figure 4(a) shows the best-fit potential functions for ^{3}He and ^{4}He inside the interior cavity of C_{60}. The best-fit potential has a distinct U-shape, which deviates strongly from the parabolic form of a harmonic oscillator. The best-fit potential curves ^{3}He and ^{4}He differ by not more than ± 1 cm^{-1} over the plotted energy range.

An energy level diagram for the confined He atoms, marked with the observed transitions, is shown in Fig. 4(b). The predicted positions of the relevant THz and INS transitions are shown by the vertical bars in Figs. 2 and 3. Although some of the higher-energy transitions in the INS data are partially obscured by C_{60} features, the agreement with the spectroscopic results is gratifying. The remaining discrepancies between the experiment and theory are minor, such as the form of the peak labeled 4 in Fig. 2(a), and are currently unexplained. The close correspondence of the derived potential curves for ^{3}He and ^{4}He, despite the different masses of the isotopes and the very different observed frequencies, attests to the validity of the determination of $V(r)$.

C. Comparison with empirical potentials

There have been numerous attempts to model the nonbonded interactions between atoms using empirical two-body potential functions, such as the Lennard-Jones (LJ) 6-12 potential, or by more complex functional forms. Suitable functions and parameters have been proposed for the He···C interaction.[14,15,64,65,67] Some of the proposed two-body potentials were developed for modeling the scattering of He atoms from a graphite surface.[14,15]

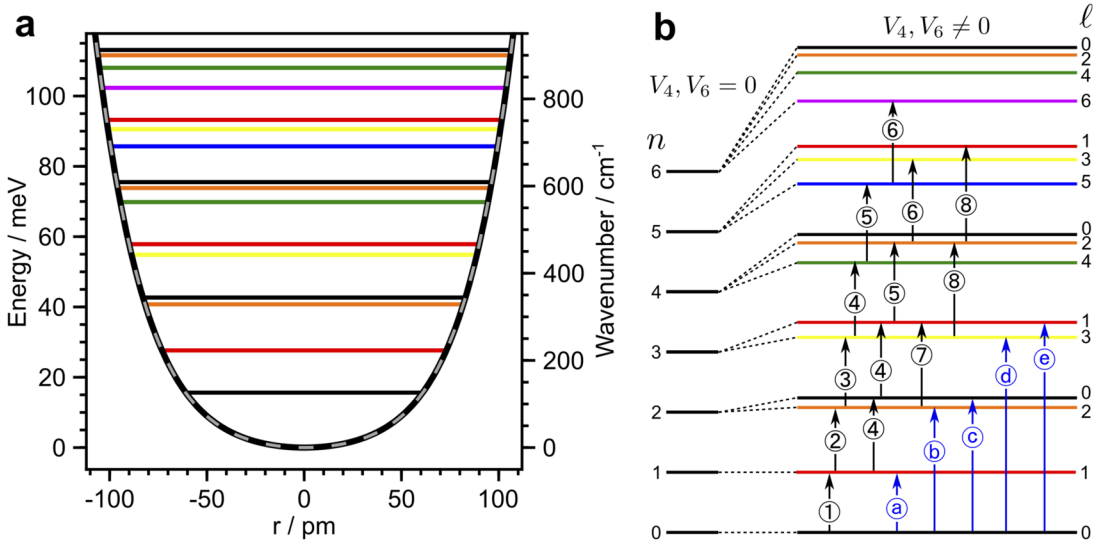

FIG. 4. (a) Radial potential energy functions $V(r)$ for ^{3}He in C_{60} (black solid curve) and for ^{4}He in C_{60} (gray dashed curve) together with the quantized energy levels for ^{3}He. The ^{3}He and ^{4}He potential curves are superposed within this energy range, leading to a "railway track" appearance of the plotted curve. The best-fit polynomial coefficients are given in Table I. (b) Energy levels of the confined ^{3}He atoms, labeled by the quantum numbers $n\ell$. The energy levels for a harmonic oscillator are shown on the left. The finite V_4 and V_6 terms break the degeneracies between terms with different ℓ. All levels are $(2\ell + 1)$-fold degenerate. The transitions observed in THz spectroscopy are labeled by circled numbers in black and correspond to the peaks in Fig. 2. The transitions observed in INS are labeled by circled letters in blue and correspond to the peaks in Fig. 3. Colors are used to indicate the ℓ values of the energy levels.

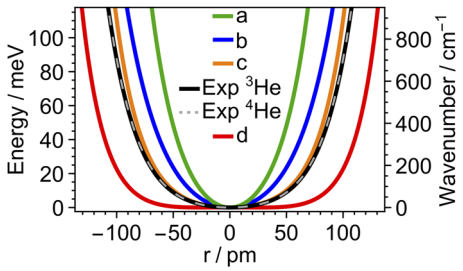

FIG. 5. Comparison of the experimentally determined radial potentials $V(r)$ (^{3}He: black solid curve; ^{4}He: gray dashed curve, superposed on the ^{3}He curve to give a "train track" appearance) with sums of reported He···C interaction potentials: [(a) green] Lennard-Jones 6-8-12 potential with parameters from Carlos and Cole;[14] [(b) blue] modified Buckingham potential (implemented in the MM3 program, as reported by Jiménez-Vázquez and Cross[64]); [(c) orange] Lennard-Jones 6-12 potential with parameters from Pang and Brisse;[65] [(d) red] Lennard-Jones 6-12 potential with parameters from Carlos and Cole.[14] The potentials used in (a) and (d) were used for the fitting of He···C scattering data.[14] The functional forms of the potentials and their associated parameters are given in the supplementary material. In all cases, the He atom was displaced from the cage center toward the nucleus of a carbon atom. The confidence limits in the structural data for C_{60}[66] lead to error margins on the empirical curves, which are smaller than the plotted linewidths.

Figure 5 compares the experimental $V(r)$ curve with predictions from published He···C two-body interaction functions. In each case, the total potential energy $V(r)$ was estimated by locating the He atom at a distance r along a line from the center of the cage toward a C atom and summing the contributions from all 60 two-body He···C potentials. The direction of the He displacement has a negligible effect on the calculated potential curves over the relevant energy range (see the supplementary material). The derived potentials are very sensitive to the geometry of the C_{60} cage, especially its radius R. We fixed the locations of all C nuclei to the best current estimates from neutron diffraction[66] as follows: bond lengths $h = 138.14 \pm 0.27$ pm for C–C bonds shared by two hexagons, $p = 145.97 \pm 0.18$ pm for C–C bonds shared by a hexagon and a pentagon, and distance of all carbon atoms from the cage center $R = 354.7 \pm 0.5$ pm. The width of the curves in Fig. 5 is greater than their confidence limits, which are dominated by the uncertainties in the structural parameters. Explicit functional forms and parameters for the empirical two-body potentials are given in the supplementary material.

The most striking feature of Fig. 5 is the wide variation in derived potentials for different two-body interaction models. Of all the proposed two-body potentials, the Lennard-Jones 6-12 potential with parameters given by Pang and Brisse[65] [curve (c)] provides the best agreement with the experiment. The isotropic two-body potentials derived by fitting the experimental He/graphite scattering data[14,15] [curves (a) and (d)] give poor fits to the experimental He@C_{60} potential.

D. Comparison with quantum chemistry

The He@C_{60} system is too large to be treated at the full *ab initio* level of quantum chemistry. The availability of an experimental radial potential function $V(r)$ allows the direct evaluation of approximate computational chemistry techniques—not only at the equilibrium geometry but also for displacements of the He atom from the center of the C_{60} cage.

The radial potential $V(r)$ was evaluated by estimating the energy of a He@C_{60} system using a range of computational chemistry algorithms with the He atom displaced by r from the center of the C_{60} cage. In all cases, the locations of the carbon atoms were fixed to the C_{60} geometry as determined by neutron diffraction[66] with the same parameters as used for the evaluation of the empirical potentials. The He atom was moved on the line connecting the cage center to a carbon nucleus. The direction of the He displacement has a negligible effect on the predicted potential curves over the relevant energy range (see the supplementary material). The potentials were calculated using the Psi4 program.[68] The functionals used for DFT were (i) the B3LYP functional, which is one of the most popular semi-empirical hybrid functionals;[69–73] (ii) the B3LYP functional, including the Grimme D3 empirical dispersion correction with Beck–Johnson damping;[5,74] (iii) the ωB97X-V functional, which includes a contribution from the nonlocal VV10 correlation functional and is designed to handle non-covalent interactions.[69] The potential was also calculated using second-order Møller–Plesset perturbation (MP2) theory,[2] including empirical spin-component-scaling (SCS) factors.[75] All potential calculations employed a counterpoise basis-set-superposition-error correction and converged to a good approximation with the correlation-consistent cc-pVXZ (X = D, T, Q, 5) basis sets.[76,77] The calculations with $X = Q$ and $X = 5$ were found to agree within 1% in the case of MP2 theory and within 7% for the two DFT-functionals. More details on the quantum chemistry calculations are given in the supplementary material.

Some comparisons are shown in Fig. 6. Density functional theory with the popular B3LYP functional[69–73] overestimates the steepness of the confining potential, although the correspondence with the experiment is improved by including the empirical D3

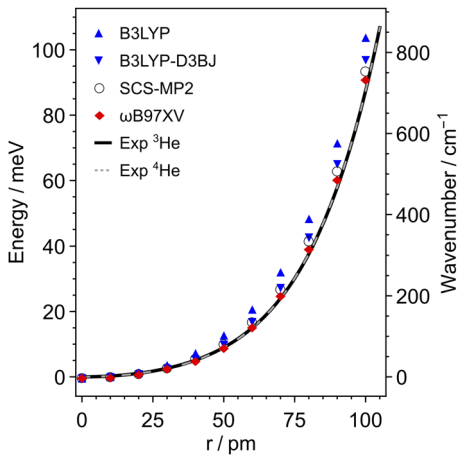

FIG. 6. Comparison of the experimentally determined He@C_{60} radial potentials $V(r)$ (^{3}He: black solid curve; ^{4}He: gray dashed curve, superposed on the ^{3}He curve) with quantum chemical calculations using density functional and Møller–Plesset perturbation theories[2] as follows: (blue upper triangle) DFT using the B3LYP functional;[70–73] (blue lower triangle) DFT using the B3LYP functional with D3BJ correction;[5,74] (red diamond) DFT using the ωB97XV functional;[69,78] and (open circle) spin-component-scaled Møller–Plesset perturbation theory (SCS-MP2).[75]

correction with Beck–Johnson damping.[5,74] DFT with the ωB97X-V functional[69] and Møller–Plesset perturbation (MP2) theory with spin-component-scaling (SCS) factors[75] give an acceptable correspondence between the calculated and experimentally determined potentials.

V. DISCUSSION

We have showed that the quantized energy levels of helium atoms encapsulated in C_{60} cages may be probed by THz spectroscopy and INS, despite the weak interactions of the He atoms with the electromagnetic field and with neutrons. The spectroscopic features were analyzed to obtain a detailed potential energy function for the interaction between the encapsulated species and the surrounding cage—an interaction dominated by nonbonded dispersion forces, which are hard to estimate experimentally. An excellent correspondence was obtained between the interaction potentials derived from independent ^{3}He@C_{60} and ^{4}He@C_{60} measurements, despite the different peak positions for the two samples.

The experimental $V(r)$ curve was compared with sums of published two-body He···C interactions. With a few exceptions, the summed two-body potentials have a poor correspondence with the experimental result. It is not a great surprise that the interaction of a He atom with a highly delocalized electronic structure such as C_{60} is hard to model as the sum of individual atom–atom interactions.

We also compared the experimentally derived interaction potential with those derived by quantum chemistry techniques. This allowed the validation of DFT methods that have been developed to deal with dispersive interactions, including the popular B3LYP functional with the D3 empirical dispersion correction[5,74] and the ωB97X-V functional, which incorporates the nonlocal VV10 correlation functional and has been parameterized using a training set rich in nonbonding interactions.[69] Møller–Plesset perturbation theory with spin-component-scaling factors[75] also provides a good description of the confining potential of the encapsulated He atoms.

There are small discrepancies between the calculated and observed potentials. However, it is not yet known whether the remaining discrepancies reflect the limitations in the quantum chemistry algorithms or the limitations in the assumptions made when interpreting the experimental data—for example, the neglect of the influence exerted by the encapsulated He atoms on the cage radius. Precise measurements of the He@C_{60} cage geometry by neutron scattering or x-ray diffraction are planned.

He atoms are small, have no static dipole moment, and have low polarizability. This makes He@C_{60} a relatively easy case for computational chemistry. A stiffer challenge for computational chemistry is likely to be presented by compounds in which the endohedral species is polar, such as H_2O@C_{60}[24] and HF@C_{60},[22] and by endofullerenes such as CH_4@C_{60},[23] where the fit with the cage is much tighter. Furthermore, the study of the systems with multiple atoms or molecules encapsulated in the same fullerene cage[24,26,27] should allow the study of nonbonded molecule–molecule and molecule–atom interactions.

SUPPLEMENTARY MATERIAL

The supplementary material includes technical details of the terahertz spectroscopy; technical details of the inelastic neutron scattering measurements; quantum theory of a confined atom in a spherical potential, including fitting procedures for the confining potential; details of the two-body potentials; and technical details of the computational chemistry calculations.

ACKNOWLEDGMENTS

This research was supported by EPSRC-UK (Grant Nos. EP/P009980/1, EP/T004320/1, and EP/P030491/1), the Estonian Ministry of Education and Research institutional research funding IUT23-3 and personal research funding PRG736, European Regional Development Fund Project No. TK134, and the European Union's Horizon 2020 research and innovation program under Marie Skłodowska-Curie Grant Agreement No. 891400. The Institut Laue-Langevin is acknowledged for providing neutron beam time and support for M.A. through the ILL Ph.D. program. The authors acknowledge the use of the IRIDIS High Performance Computing Facility and associated support services at the University of Southampton in the completion of this work.

AUTHOR DECLARATIONS

Conflict of Interest

The authors have no conflicts to disclose.

Author Contributions

G.R.B. conceived the THz experiments. M.W., G.H., and R.J.W. synthesized and purified the compounds. G.R.B., T.J., A.S., U.N., and T.R. performed the THz experiments and processed the THz data. A.J.H. and S.R. designed the INS experiments. G.R.B., M.A., and S.R. performed the INS experiments and processed the INS data. G.R.B., M.A., and T.R. derived the potential function. J.R. and R.J.W. performed the quantum chemistry calculations. G.R.B., M.A., J.R., A.J.H., S.R., T.R., R.J.W., and M.H.L. developed the concept and drafted this paper. All authors reviewed the manuscript.

DATA AVAILABILITY

The data that support the findings of this study are available from the corresponding author upon reasonable request.

REFERENCES

[1] D. Wales, *Energy Landscapes: Applications to Clusters, Biomolecules and Glasses*, Cambridge Molecular Science (Cambridge University Press, Cambridge, 2004).
[2] F. Jensen, *Introduction to Computational Chemistry*, 3rd ed. (Wiley, Chichester, 2017).
[3] M. Waller and S. Grimme, "Weak intermolecular interactions: A supermolecular approach," in *Handbook of Computational Chemistry*, edited by J. Leszczynski (Springer Netherlands, Dordrecht, 2016), pp. 1–27.
[4] Y. Shao, Z. Gan, E. Epifanovsky, A. T. B. Gilbert, M. Wormit, J. Kussmann, A. W. Lange, A. Behn, J. Deng, X. Feng, D. Ghosh, M. Goldey, P. R. Horn, L. D. Jacobson, I. Kaliman, R. Z. Khaliullin, T. Kuś, A. Landau, J. Liu, E. I. Proynov, Y. M. Rhee, R. M. Richard, M. A. Rohrdanz, R. P. Steele, E. J. Sundstrom, H. Lee Woodcock III, P. M. Zimmerman, D. Zuev, B. Albrecht, E. Alguire, B. Austin, G. J. O. Beran, Y. A. Bernard, E. Berquist, K. Brandhorst, K. B. Bravaya, S. T. Brown, D. Casanova, C.-M. Chang, Y. Chen, S. H. Chien, K. D. Closser, D. L. Crittenden, M. Diedenhofen, R. A. DiStasio, Jr., H. Do, A. D. Dutoi, R. G. Edgar, S. Fatehi, L. Fusti-Molnar, A. Ghysels, A. Golubeva-Zadorozhnaya, J. Gomes, M. W. D. Hanson-Heine, P. H. P. Harbach, A. W. Hauser, E. G. Hohenstein, Z. C. Holden, T.-C. Jagau, H. Ji, B. Kaduk, K. Khistyaev, J. Kim, J. Kim, R. A. King,

P. Klunzinger, D. Kosenkov, T. Kowalczyk, C. M. Krauter, K. U. Lao, A. D. Laurent, K. V. Lawler, S. V. Levchenko, C. Y. Lin, F. Liu, E. Livshits, R. C. Lochan, A. Luenser, P. Manohar, S. F. Manzer, S.-P. Mao, N. Mardirossian, A. V. Marenich, S. A. Maurer, N. J. Mayhall, E. Neuscamman, C. M. Oana, R. Olivares-Amaya, D. P. O'Neill, J. A. Parkhill, T. M. Perrine, R. Peverati, A. Prociuk, D. R. Rehn, E. Rosta, N. J. Russ, S. M. Sharada, S. Sharma, D. W. Small, A. Sodt, T. Stein, D. Stück, Y.-C. Su, A. J. W. Thom, T. Tsuchimochi, V. Vanovschi, L. Vogt, O. Vydrov, T. Wang, M. A. Watson, J. Wenzel, A. White, C. F. Williams, J. Yang, S. Yeganeh, S. R. Yost, Z.-Q. You, I. Y. Zhang, X. Zhang, Y. Zhao, B. R. Brooks, G. K. L. Chan, D. M. Chipman, C. J. Cramer, W. A. Goddard III, M. S. Goddard, W. J. Hehre, A. Klamt, H. F. Schaefer III, M. W. Schmidt, C. D. Sherrill, D. G. Truhlar, A. Warshel, X. Xu, A. Aspuru-Guzik, R. Baer, A. T. Bell, N. A. Besley, J.-D. Chai, A. Dreuw, B. D. Dunietz, T. R. Furlani, S. R. Gwaltney, C.-P. Hsu, Y. Jung, J. Kong, D. S. Lambrecht, W. Liang, C. Ochsenfeld, V. A. Rassolov, L. V. Slipchenko, J. E. Subotnik, T. Van Voorhis, J. M. Herbert, A. I. Krylov, P. M. W. Gill, and M. Head-Gordon, "Advances in molecular quantum chemistry contained in the Q-Chem 4 program package," Mol. Phys. **113**, 184–215 (2015).

[5]S. Grimme, J. Antony, S. Ehrlich, and H. Krieg, "A consistent and accurate *ab initio* parametrization of density functional dispersion correction (DFT-D) for the 94 elements H-Pu," J. Chem. Phys. **132**, 154104 (2010).

[6]F. A. Momany, L. M. Carruthers, R. F. McGuire, and H. A. Scheraga, "Intermolecular potentials from crystal data. III. Determination of empirical potentials and application to the packing configurations and lattice energies in crystals of hydrocarbons, carboxylic acids, amines, and amides," J. Phys. Chem. **78**, 1595–1620 (1974).

[7]F. N. Keutsch and R. J. Saykally, "Water clusters: Untangling the mysteries of the liquid, one molecule at a time," Proc. Natl. Acad. Sci. U. S. A. **98**, 10533–10540 (2001).

[8]P. Hobza and K. Muller-Dethlefs, *Non-Covalent Interactions: Theory and Experiment* (The Royal Society of Chemistry, 2009).

[9]L. Zhu and P. Johnson, "Mass analyzed threshold ionization spectroscopy," J. Chem. Phys. **94**, 5769–5771 (1991).

[10]H. Krause and H. J. Neusser, "Dissociation energy of neutral and ionic benzene-noble gas dimers by pulsed field threshold ionization spectroscopy," J. Chem. Phys. **99**, 6278–6286 (1993).

[11]A. Van Orden and R. J. Saykally, "Small carbon clusters: Spectroscopy, structure, and energetics," Chem. Rev. **98**, 2313–2358 (1998).

[12]T. P. Softley, "Applications of molecular Rydberg states in chemical dynamics and spectroscopy," Int. Rev. Phys. Chem. **23**, 1–78 (2004).

[13]D. Farias and K.-H. Rieder, "Atomic beam diffraction from solid surfaces," Rep. Prog. Phys. **61**, 1575–1664 (1998).

[14]W. E. Carlos and M. W. Cole, "Interaction between a He atom and a graphite surface," Surf. Sci. **91**, 339–357 (1980).

[15]M. W. Cole, D. R. Frankl, and D. L. Goodstein, "Probing the helium-graphite interaction," Rev. Mod. Phys. **53**, 199–210 (1981).

[16]M. Saunders, H. A. Jimenez-Vazquez, R. J. Cross, and R. J. Poreda, "Stable compounds of helium and neon: He@C_{60} and Ne@C_{60}," Science **259**, 1428–1430 (1993).

[17]M. Saunders, R. J. Cross, H. A. Jimenez-Vazquez, R. Shimshi, and A. Khong, "Noble gas atoms inside fullerenes," Science **271**, 1693–1697 (1996).

[18]K. Komatsu, M. Murata, and Y. Murata, "Encapsulation of molecular hydrogen in fullerene C_{60} by organic synthesis," Science **307**, 238–240 (2005).

[19]K. Kurotobi and Y. Murata, "A single molecule of water encapsulated in fullerene C_{60}," Science **333**, 613–616 (2011).

[20]Y. Rubin, T. Jarrosson, G.-W. Wang, M. D. Bartberger, K. N. Houk, G. Schick, M. Saunders, and R. J. Cross, "Insertion of helium and molecular hydrogen through the orifice of an open fullerene," Angew. Chem., Int. Ed. **40**, 1543–1546 (2001).

[21]M. Murata, S. Maeda, Y. Morinaka, Y. Murata, and K. Komatsu, "Synthesis and reaction of fullerene C_{70} encapsulating two molecules of H_2," J. Am. Chem. Soc. **130**, 15800–15801 (2008).

[22]A. Krachmalnicoff, R. Bounds, S. Mamone, S. Alom, M. Concistrè, B. Meier, K. Kouřil, M. E. Light, M. R. Johnson, S. Rols, A. J. Horsewill, A. Shugai, U. Nagel, T. Rõõm, M. Carravetta, M. H. Levitt, and R. J. Whitby, "The dipolar endofullerene HF@C_{60}," Nat. Chem. **8**, 953–957 (2016).

[23]S. Bloodworth, G. Sitinova, S. Alom, S. Vidal, G. R. Bacanu, S. J. Elliott, M. E. Light, J. M. Herniman, G. J. Langley, M. H. Levitt, and R. J. Whitby, "First synthesis and characterization of CH_4@C_{60}," Angew. Chem., Int. Ed. **58**, 5038–5043 (2019).

[24]Y. Murata, S. Maeda, M. Murata, and K. Komatsu, "Encapsulation and dynamic behavior of two H_2 molecules in an open-cage C_{70}," J. Am. Chem. Soc. **130**, 6702–6703 (2008).

[25]Y. Morinaka, F. Tanabe, M. Murata, Y. Murata, and K. Komatsu, "Rational synthesis, enrichment, and ^{13}C NMR spectra of endohedral C_{60} and C_{70} encapsulating a helium atom," Chem. Commun. **46**, 4532–4534 (2010).

[26]R. Zhang, M. Murata, T. Aharen, A. Wakamiya, T. Shimoaka, T. Hasegawa, and Y. Murata, "Synthesis of a distinct water dimer inside fullerene C_{70}," Nat. Chem. **8**, 435–441 (2016).

[27]R. Zhang, M. Murata, A. Wakamiya, T. Shimoaka, T. Hasegawa, and Y. Murata, "Isolation of the simplest hydrated acid," Sci. Adv. **3**, e1602833 (2017).

[28]S. Bloodworth, G. Hoffman, M. C. Walkey, G. R. Bacanu, J. M. Herniman, M. H. Levitt, and R. J. Whitby, "Synthesis of Ar@C_{60} using molecular surgery," Chem. Commun. **56**, 10521–10524 (2020).

[29]G. R. Bacanu, J. Rantaharju, G. Hoffman, M. C. Walkey, S. Bloodworth, M. Concistrè, R. J. Whitby, and M. H. Levitt, "An internuclear *J*-coupling of ^{3}He induced by molecular confinement," J. Am. Chem. Soc. **142**, 16926–16929 (2020).

[30]G. Hoffman, M. C. Walkey, J. Gräsvik, G. R. Bacanu, S. Alom, S. Bloodworth, M. E. Light, M. H. Levitt, and R. J. Whitby, "A solid state intramolecular Wittig reaction enables efficient synthesis of endofullerenes including Ne@C_{60}, ^{3}He@C_{60} and HD@C_{60}," Angew. Chem., Int. Ed. **60**, 8960–8966 (2021).

[31]M. H. Levitt, "Spectroscopy of light-molecule endofullerenes," Philos. Trans. R. Soc., A **371**, 20120429 (2013).

[32]S. Mamone, M. Ge, D. Hüvonen, U. Nagel, A. Danquigny, F. Cuda, M. C. Grossel, Y. Murata, K. Komatsu, M. H. Levitt, T. Rõõm, and M. Carravetta, "Rotor in a cage: Infrared spectroscopy of an endohedral hydrogen-fullerene complex," J. Chem. Phys. **130**, 081103–081104 (2009).

[33]M. Ge, U. Nagel, D. Hüvonen, T. Rõõm, S. Mamone, M. H. Levitt, M. Carravetta, Y. Murata, K. Komatsu, X. Lei, and N. J. Turro, "Infrared spectroscopy of endohedral HD and D_2 in C_{60}," J. Chem. Phys. **135**, 114511 (2011).

[34]C. Beduz, M. Carravetta, J. Y. C. Chen, M. Concistré, M. Denning, M. Frunzi, A. J. Horsewill, O. G. Johannessen, R. Lawler, X. Lei, M. H. Levitt, Y. Li, S. Mamone, Y. Murata, U. Nagel, T. Nishida, J. Ollivier, S. Rols, T. Rõõm, R. Sarkar, N. J. Turro, and Y. Yang, "Quantum rotation of *ortho* and *para*-water encapsulated in a fullerene cage," Proc. Natl. Acad. Sci. U. S. A. **109**, 12894–12898 (2012).

[35]T. Rõõm, L. Peedu, M. Ge, D. Hüvonen, U. Nagel, S. Ye, M. Xu, Z. Bačić, S. Mamone, M. H. Levitt, M. Carravetta, J. Y.-C. Chen, X. Lei, N. J. Turro, Y. Murata, and K. Komatsu, "Infrared spectroscopy of small-molecule endofullerenes," Philos. Trans. R. Soc., A **371**, 20110631 (2013).

[36]A. Shugai, U. Nagel, Y. Murata, Y. Li, S. Mamone, A. Krachmalnicoff, S. Alom, R. J. Whitby, M. H. Levitt, and T. Rõõm, "Infrared spectroscopy of an endohedral water in fullerene," J. Chem. Phys. **154**, 124311 (2021).

[37]S. S. Zhukov, V. Balos, G. Hoffman, S. Alom, M. Belyanchikov, M. Nebioglu, S. Roh, A. Pronin, G. R. Bacanu, P. Abramov, M. Wolf, M. Dressel, M. H. Levitt, R. J. Whitby, B. Gorshunov, and M. Sajadi, "Rotational coherence of encapsulated ortho and para water in fullerene-C_{60} revealed by time-domain terahertz spectroscopy," Sci. Rep. **10**, 18329 (2020).

[38]N. J. Turro, J. Y. C. Chen, E. Sartori, M. Ruzzi, A. Marti, R. Lawler, S. Jockusch, J. López-Gejo, K. Komatsu, and Y. Murata, "The spin chemistry and magnetic resonance of H_2@C_{60}. From the Pauli principle to trapping a long lived nuclear excited spin state inside a buckyball," Acc. Chem. Res. **43**, 335 (2009).

[39]S. Mamone, M. Concistrè, I. Heinmaa, M. Carravetta, I. Kuprov, G. Wall, M. Denning, X. Lei, J. Y.-C. Chen, Y. Li, Y. Murata, N. J. Turro, and M. H. Levitt, "Nuclear magnetic resonance of hydrogen molecules trapped inside C_{70} fullerene cages," ChemPhysChem **14**, 3121–3130 (2013).

[40]G. R. Bacanu, G. Hoffman, M. Amponsah, M. Concistrè, R. J. Whitby, and M. H. Levitt, "Fine structure in the solution state ^{13}C-NMR spectrum of C_{60} and its endofullerene derivatives," Phys. Chem. Chem. Phys. **22**, 11850–11860 (2020).

[41]A. J. Horsewill, K. S. Panesar, S. Rols, J. Ollivier, M. R. Johnson, M. Carravetta, S. Mamone, M. H. Levitt, Y. Murata, K. Komatsu, J. Y.-C. Chen, J. A. Johnson, X. Lei, and N. J. Turro, "Inelastic neutron scattering investigations of the quantum

molecular dynamics of a H_2 molecule entrapped inside a fullerene cage," Phys. Rev. B **85**, 205440 (2012).
[42]S. Mamone, M. R. Johnson, J. Ollivier, S. Rols, M. H. Levitt, and A. J. Horsewill, "Symmetry-breaking in the H_2@C_{60} endofullerene revealed by inelastic neutron scattering at low temperature," Phys. Chem. Chem. Phys. **18**, 1998–2005 (2016).
[43]S. Mamone, M. Jiménez-Ruiz, M. R. Johnson, S. Rols, and A. J. Horsewill, "Experimental, theoretical and computational investigation of the inelastic neutron scattering spectrum of a homonuclear diatomic molecule in a nearly spherical trap: H_2@C_{60}," Phys. Chem. Chem. Phys. **18**, 29369–29380 (2016).
[44]M. Xu, F. Sebastianelli, Z. Bačić, R. Lawler, and N. J. Turro, "H_2, HD, and D_2 inside C_{60}: Coupled translation-rotation eigenstates of the endohedral molecules from quantum five-dimensional calculations," J. Chem. Phys. **129**, 064313 (2008).
[45]M. Xu, F. Sebastianelli, Z. Bačić, R. Lawler, and N. J. Turro, "Quantum dynamics of coupled translational and rotational motions of H_2 inside C_{60}," J. Chem. Phys. **128**, 011101–011104 (2008).
[46]M. Xu, F. Sebastianelli, B. R. Gibbons, Z. Bačić, R. Lawler, and N. J. Turro, "Coupled translation-rotation eigenstates of H_2 in C_{60} and C_{70} on the spectroscopically optimized interaction potential: Effects of cage anisotropy on the energy level structure and assignments," J. Chem. Phys. **130**, 224306 (2009).
[47]M. Ge, U. Nagel, D. Hüvonen, T. Rõõm, S. Mamone, M. H. Levitt, M. Carravetta, Y. Murata, K. Komatsu, J. Y.-C. Chen, and N. J. Turro, "Interaction potential and infrared absorption of endohedral H_2 in C_{60}," J. Chem. Phys. **134**, 054507 (2011).
[48]S. Mamone, J. Y.-C. Chen, R. Bhattacharyya, M. H. Levitt, R. G. Lawler, A. J. Horsewill, T. Rõõm, Z. Bačić, and N. J. Turro, "Theory and spectroscopy of an incarcerated quantum rotor: The infrared spectroscopy, inelastic neutron scattering and nuclear magnetic resonance of H_2@C_{60} at cryogenic temperature," Coord. Chem. Rev. **255**, 938–948 (2011).
[49]M. Xu, S. Ye, A. Powers, R. Lawler, N. J. Turro, and Z. Bačić, "Inelastic neutron scattering spectrum of H_2@C_{60} and its temperature dependence decoded using rigorous quantum calculations and a new selection rule," J. Chem. Phys. **139**, 064309 (2013).
[50]P. M. Felker and Z. Bačić, "Communication: Quantum six-dimensional calculations of the coupled translation-rotation eigenstates of H_2O@C_{60}," J. Chem. Phys. **144**, 201101 (2016).
[51]P. M. Felker, V. Vlček, I. Hietanen, S. FitzGerald, D. Neuhauser, and Z. Bačić, "Explaining the symmetry breaking observed in the endofullerenes H_2@C_{60}, HF@C_{60}, and H_2O@C_{60}," Phys. Chem. Chem. Phys. **19**, 31274–31283 (2017).
[52]Z. Bačić, "Perspective: Accurate treatment of the quantum dynamics of light molecules inside fullerene cages: Translation-rotation states, spectroscopy, and symmetry breaking," J. Chem. Phys. **149**, 100901 (2018).
[53]Z. Bačić, M. Xu, and P. M. Felker, "Coupled translation–rotation dynamics of H_2 and H_2O inside C_{60}: Rigorous quantum treatment," in *Advances in Chemical Physics* (Wiley-Blackwell, 2018), pp. 195–216.
[54]M. Xu, P. M. Felker, S. Mamone, A. J. Horsewill, S. Rols, R. J. Whitby, and Z. Bačić, "The endofullerene HF@C_{60}: Inelastic neutron scattering spectra from quantum simulations and experiment, validity of the selection rule, and symmetry breaking," J. Phys. Chem. Lett. **10**, 5365–5371 (2019).
[55]P. M. Felker and Z. Bačić, "Flexible water molecule in C_{60}: Intramolecular vibrational frequencies and translation-rotation eigenstates from fully coupled nine-dimensional quantum calculations with small basis sets," J. Chem. Phys. **152**, 014108 (2020).
[56]M. Xu, P. M. Felker, and Z. Bačić, "Light molecules inside the nanocavities of fullerenes and clathrate hydrates: Inelastic neutron scattering spectra and the unexpected selection rule from rigorous quantum simulations," Int. Rev. Phys. Chem. **39**, 425–463 (2020).
[57]D. E. Giblin, M. L. Gross, M. Saunders, H. Jimenez-Vazquez, and R. J. Cross, "Incorporation of helium into endohedral complexes of C_{60} and C_{70} containing noble-gas atoms: A tandem mass spectrometry study," J. Am. Chem. Soc. **119**, 9883–9890 (1997).
[58]S. Rols, C. Bousige, J. Cambedouzou, P. Launois, J.-L. Sauvajol, H. Schober, V. N. Agafonov, V. A. Davydov, and J. Ollivier, "Unravelling low lying phonons and vibrations of carbon nanostructures: The contribution of inelastic and quasi-elastic neutron scattering," Eur. Phys. J.: Spec. Top. **213**, 77–102 (2012).
[59]F. Cimpoesu, S. Ito, H. Shimotani, H. Takagi, and N. Dragoe, "Vibrational properties of noble gas endohedral fullerenes," Phys. Chem. Chem. Phys. **13**, 9609–9615 (2011).
[60]C. Cohen-Tannoudji, B. Diu, and F. Laloë, *Quantum Mechanics*, 2nd ed. (Wiley-VCH, 2020).
[61]W. H. Shaffer, "Degenerate modes of vibration and perturbations in polyatomic molecules," Rev. Mod. Phys. **16**, 245–259 (1944).
[62]S. Flügge, *Practical Quantum Mechanics*, Classics in Mathematics (Springer-Verlag, Berlin, Heidelberg, 1999).
[63]B. H. Bransden and C. J. Joachain, *Quantum Mechanics*, 2nd ed. (Pearson Prentice Hall, 2000).
[64]H. A. Jiménez-Vázquez and R. J. Cross, "Equilibrium constants for noble-gas fullerene compounds," J. Chem. Phys. **104**, 5589–5593 (1996).
[65]L. Pang and F. Brisse, "Endohedral energies and translation of fullerene-noble gas clusters G@Cn (G = helium, neon, argon, krypton and xenon; n = 60 and 70)," J. Phys. Chem. **97**, 8562–8563 (1993).
[66]F. Leclercq, P. Damay, M. Foukani, P. Chieux, M. C. Bellissent-Funel, A. Rassat, and C. Fabre, "Precise determination of the molecular geometry in fullerene C_{60} powder: A study of the structure factor by neutron scattering in a large momentum-transfer range," Phys. Rev. B **48**, 2748–2758 (1993).
[67]A. Terry Amos, T. Frank Palmer, A. Walters, and B. L. Burrows, "Atom–atom potential parameters for van der Waals complexes of aromatics and rare-gas atoms," Chem. Phys. Lett. **172**, 503–508 (1990).
[68]R. M. Parrish, L. A. Burns, D. G. A. Smith, A. C. Simmonett, A. E. DePrince III, E. G. Hohenstein, U. Bozkaya, A. Y. Sokolov, R. Di Remigio, R. M. Richard *et al.*, "Psi4 1.1: An open-source electronic structure program emphasizing automation, advanced libraries, and interoperability," J. Chem. Theory Comput. **13**, 3185–3197 (2017).
[69]N. Mardirossian and M. Head-Gordon, "Thirty years of density functional theory in computational chemistry: An overview and extensive assessment of 200 density functionals," Mol. Phys. **115**, 2315–2372 (2017).
[70]C. Lee, W. Yang, and R. G. Parr, "Development of the Colle-Salvetti correlation-energy formula into a functional of the electron density," Phys. Rev. B **37**, 785–789 (1988).
[71]S. H. Vosko, L. Wilk, and M. Nusair, "Accurate spin-dependent electron liquid correlation energies for local spin density calculations: A critical analysis," Can. J. Phys. **58**, 1200–1211 (1980).
[72]A. D. Becke, "Density-functional thermochemistry. III. The role of exact exchange," J. Chem. Phys. **98**, 5648–5652 (1993).
[73]P. J. Stephens, F. J. Devlin, C. F. Chabalowski, and M. J. Frisch, "Ab initio calculation of vibrational absorption and circular dichroism spectra using density functional force fields," J. Phys. Chem. **98**, 11623–11627 (1994).
[74]S. Grimme, S. Ehrlich, and L. Goerigk, "Effect of the damping function in dispersion corrected density functional theory," J. Comput. Chem. **32**, 1456–1465 (2011).
[75]S. Grimme, "Improved second-order Møller–Plesset perturbation theory by separate scaling of parallel- and antiparallel-spin pair correlation energies," J. Chem. Phys. **118**, 9095–9102 (2003).
[76]T. H. Dunning, Jr., "Gaussian basis sets for use in correlated molecular calculations. I. The atoms boron through neon and hydrogen," J. Chem. Phys. **90**, 1007–1023 (1989).
[77]D. E. Woon and T. H. Dunning, Jr., "Gaussian basis sets for use in correlated molecular calculations. IV. Calculation of static electrical response properties," J. Chem. Phys. **100**, 2975–2988 (1994).
[78]N. Mardirossian and M. Head-Gordon, "ωb97X-V: A 10-parameter, range-separated hybrid, generalized gradient approximation density functional with nonlocal correlation, designed by a survival-of-the-fittest strategy," Phys. Chem. Chem. Phys. **16**, 9904–9924 (2014).